Computational design and experimental validation of monometallic-doped SnO$_2$ catalysts for selective catalytic oxidation of ammonia

Yan Zhang [a,b], Min Zhang [a,b], Meng Wang [a,b], Caixia Liu [a,b,*], Qingling Liu [a,b], Weichao Wang [c], Ziyin Zhang [d,e,f], Rui Han [a], Na Ji [a]

[a] School of Environmental Science and Engineering, Tianjin University, Tianjin 300350, China
[b] State Key Laboratory of Engines, School of Mechanical Engineering, Tianjin University, Tianjin 300350, China
[c] College of Environmental Science and Engineering, Tianjin Key Laboratory of Environmental Remediation & Pollution Control, MOE Key Laboratory of Pollution Processes and Environmental Criteria, Nankai University, Tianjin 300350, China
[d] Langfang City Beichen Entrepreneurship Resin Materials Incorporated Company, Langfang 065000, China
[e] Hebei Province New Resin Material Technology Innovation Center, Langfang 065000, China
[f] New Catalytic Materials Engineering Research Center for Air Pollutant Control, Langfang 065000, China

ARTICLE INFO

ABSTRACT

Due to the intricate structure of catalysts, traditional catalyst design relies on iterative trial-and-error experiments. We have systematically established a catalyst design strategy to evaluate the performance of NH$_3$-SCO reactions from the perspective of DFT calculations. Specifically, we used the catalyst formation energy as a stability descriptor and the adsorption energies of NH$_3$, NH$_2$, and O p-band center as performance descriptors, we identified the four most promising catalysts among 45 kinds of doped SnO$_2$ catalysts. Subsequently, experimental validation was performed to demonstrate the outstanding consistency between the DFT-driven descriptors and the stability and catalytic performance of the catalyst. Particularly, the Ce doping resulted in a 175 °C reduction in the T$_{90}$ compared to the SnO$_2$ catalyst. It is noteworthy that Ce doping promotes the cycling between oxygen vacancies and lattice oxygen, which contributes primarily to the enhancement of O$_2$ activation capability and, consequently, the improvement in catalytic activity.

1. Introduction

With the rapid advancement of global decarbonization plans, research interest in the application of ammonia in the energy system has been increasing [1–3]. Ammonia is a green, renewable fuel with non-carbon properties and higher hydrogen energy density [4]. Therefore, substituting diesel with ammonia fuel provides an optimal solution for decarbonizing engines to achieve greenhouse gas emission targets and mitigate global warming trends [5]. However, the use of ammonia fuel exacerbates the issue of ammonia leakage, resulting in pollution such as haze and photochemical smog, as well as posing serious health hazards [6–8]. Currently, the selective catalytic oxidation of ammonia (NH$_3$-SCO) technology is the most promising method for removing low-concentration ammonia [9,10]. Various types of NH$_3$-SCO catalysts have been studied, categorized into noble metal catalysts (Pt, Ag, Ru, Pd, etc.) and transition metal catalysts (Cu, Fe, Ce, etc.) based on different active components [11–16]. However, in practical applications,

achieving low-temperature high activity often leads to over-oxidation of ammonia, resulting in the formation of byproducts such as NO, NO$_2$, and N$_2$O, making it challenging to achieve selective ammonia removal [17]. Furthermore, considering the high-temperature and water vapor content in exhaust gases, the stability and water resistance of catalysts are crucial factors to consider. Thus, it is crucial to develop NH$_3$-SCO catalysts that exhibit high activity, excellent N$_2$ selectivity, robust water resistance, and stability across a broad temperature range to facilitate the utilization of ammonia fuel in internal combustion engines. However, due to the complex structure of catalysts, traditional catalyst design heavily relies on repetitive experiments, making it difficult to quickly and effectively identify catalysts for selective ammonia removal [18].

Recently, first-principles calculations, molecular dynamics simulations, and machine learning have emerged as more convenient approaches for catalyst design [18–21]. These methods allow us to gain molecular-level insights into the interactions between the catalyst
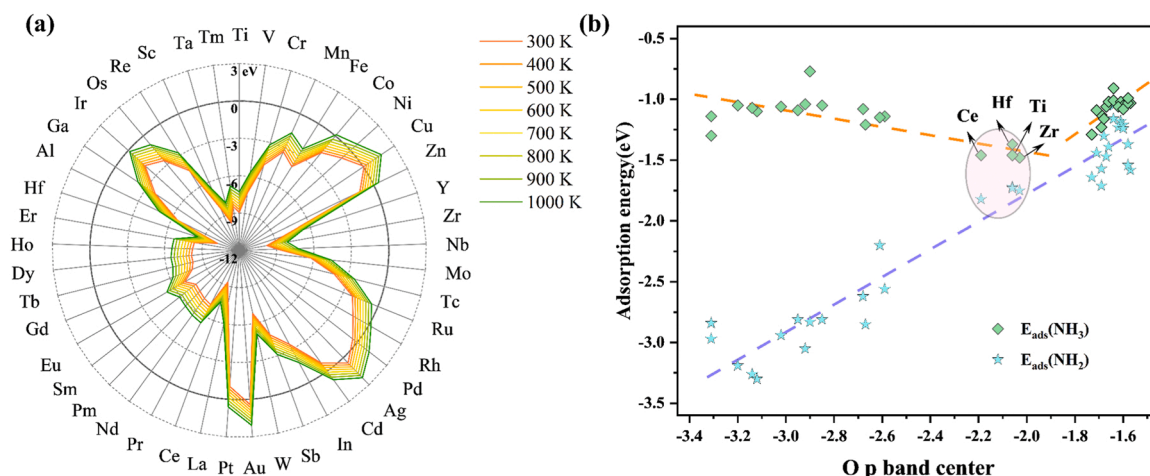

Fig. 1. (a) Formation energy of monometallic-doped SnO_2 catalysts, (b) O p-band center and adsorption energies of NH_3 and NH_2 on doped SnO_2 catalysts.

surface and reactant molecules, facilitating our understanding of catalytic processes and the development of novel catalyst design strategies. Specifically, by calculating the electronic structure, geometric configuration, adsorption energies of surface intermediates, and reaction barriers of catalysts, we can uncover the influencing factors for diverse reactions catalyzed by different catalysts. Subsequently, one or several factors, referred to as reaction descriptors, can be selected to screen catalysts suitable for a specific reaction. Since the early 20th century, the Sabatier principle has provided us with a new perspective for contemplating optimal catalysts. The Sabatier principle suggests that the best catalyst should moderately bind reactant molecules, avoiding weak binding that leads to excessively high reaction barriers or strong binding that poisons the catalyst surface [22]. Extensive research has been conducted on reaction descriptors such as d-band centers [23], p-band centers [24], and adsorption energies [25,26]. Utilizing these reaction descriptors to predict catalytic performance trends enables rational catalyst design and efficient screening of high-throughput catalysts. Therefore, it is crucial to have a clear understanding of the relationship between descriptors and catalysts, especially when employing an iterative trial-and-error approach for catalyst design.

In this paper, we illustrate a method for screening the optimal NH_3-SCO catalyst using single metal-doped SnO_2 catalysts as an example. We experimentally validate the feasibility of designing NH_3-SCO catalysts rationally using DFT-driven descriptors and further analyze the enhancement in catalytic performance attributed to O_2 activation.

2. Experimental section

2.1. Catalyst preparation

The $M_{0.1}Sn_{0.9}O_2$ catalysts (where M = Ce, Ti, Zr, Hf, Al, Sb) were prepared by co-precipitation method and named CSO, TSO, ZSO, HSO, ASO, and SSO, respectively. The CSO catalyst was prepared by dissolving 1 mmol $Ce(NO_3)_3·6H_2O$ and 9 mmol $SnCl_4$ in 100 mL of deionized water, followed by 30 min of stirring. The pH was adjusted to 9–10 by adding 1 M ammonia solution, and the mixture was stirred for 3 h and allowed to settle for 15 h. The precipitate was collected through filtration and washed with deionized water until it reached neutrality. The obtained sample was then dried at 120 °C for 12 h and calcined at 500 °C for 5 h. The preparation methods of TSO, ZSO, HSO, ASO, and SSO catalysts were similar to that of CSO, but different precursor salts were used: $Ti(SO_4)_2$, $Zr(NO_3)_4·5H_2O$, $HfCl_4$, $Al(NO_3)_3·9H_2O$, and $SbCl_3$, respectively. For the preparation of SnO_2 catalyst, 10 mmol $SnCl_4$ was dissolved in 100 mL of deionized water, and the subsequent steps were similar to the synthesis of CSO catalyst. Using a similar approach, catalytic materials $M_{0.2}Sn_{0.8}O_2$ (where M = Ce, Ti, Zr, Hf) were

synthesized, denoted as CSO-20, TSO-20, ZSO-20, and HSO-20, respectively. The hydrothermal treatment of the samples was carried out by placing the fresh catalysts in a fixed-bed reactor. A 10 % water vapor was introduced into the reaction system using a bubbling method, followed by the addition of 10 % O_2, while N_2 was used as the balance gas, and the gas flow rate was maintained at 300 mL/min. The hydrothermal treatment was performed at 700 °C for 12 h, followed by N_2 purging and cooling. The samples after hydrothermal treatment were denoted as M-A.

2.2. Catalyst characterization

Powder X-ray diffraction (XRD) analysis was conducted using a Bruker D8-Focus instrument with Cu Kα radiation. The samples were characterized for their structural and morphological properties using scanning electron microscopy (SEM, Quattro S) and high-resolution transmission electron microscopy (HR-TEM, FEI-Talos F200X). The porosity of the samples was determined through N_2 adsorption-desorption experiments performed on an Autosorb iQ instrument. X-ray photoelectron spectroscopy (XPS) measurements were carried out using a Thermo Scientific ESCALAB 250 XI electron spectrometer. NH_3-temperature-programmed-desorption (NH_3-TPD), O_2-temperature-programmed-desorption (O_2-TPD), and H_2-temperature-programmed-reduction (H_2-TPR) analyses were performed using a BSD-Chem C200 instrument from BSD INSTRUMENT, CHN. Raman spectroscopy was conducted using a Horiba LabRAM HR Evolution instrument from Horiba Jobin Yvon, FRA. In situ DRIFTS experiments were performed using a Bruker Tensor II spectrometer from Bruker, DEU. All the spin-polarized density functional theory (DFT) calculations corrected by on-site Coulomb interaction (DFT + U) were conducted by using the Vienna ab initio simulation package (VASP) [27,28]. Further details regarding the characterization procedures and computational aspects can be found in the Supporting Information (SI).

2.3. Catalytic performance evaluation

Catalytic performance tests were carried out in a fixed-bed quartz tube packed with 0.64 mL of powdered catalyst (40–60 mesh), while the concentrations of NH_3, NO, NO_2, and N_2O were measured using a Bruker Tensor II spectrometer. The gas composition consisted of 500 ppm NH_3, 10 % O_2, and 5 % H_2O (when added), with N_2 used to balance the flow at a 300 mL/min rate. The NH_3 conversion rate and selectivity for N_2, NO, NO_2, and N_2O are calculated based on the following equation.

$$NH_3\ conversion = \left(1 - \frac{[NH_3]_{out}}{[NH_3]_{in}}\right) \times 100\%$$

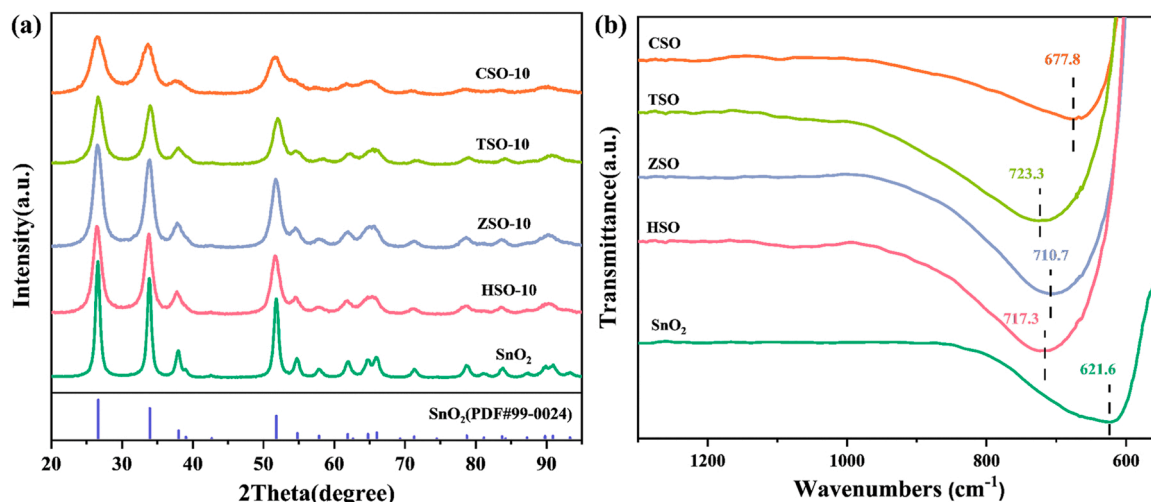$$N_2\ selectivity = \left(\frac{[NH_3]_{in} - [NO_2]_{out} - [NO]_{out} - 2[N_2O]_{out}}{[NH_3]_{in} - [NH_3]_{out}}\right) \times 100\%$$

Fig. 2. (a) XRD patterns and FTIR spectra of SnO$_2$ and (b) doped SnO$_2$ catalysts.

$$NO\ selectivity = \left(\frac{[NO]_{out}}{[NH_3]_{in} - [NH_3]_{out}}\right) \times 100\%$$

$$NO_2\ selectivity = \left(\frac{[NO_2]_{out}}{[NH_3]_{in} - [NH_3]_{out}}\right) \times 100\%$$

$$N_2O\ selectivity = \left(\frac{2[N_2O]_{out}}{[NH_3]_{in} - [NH_3]_{out}}\right) \times 100\%$$

All kinetic experiments limited the conversion of NH$_3$ to within 15 % to avoid the influence of thermodynamic factors. Initially, the effects of internal and external diffusion were eliminated through experimental procedures, followed by testing the reaction order and activation energy. For more detailed steps and calculation formulas regarding the kinetic experiments can be found in SI.

3. Results and discussion

3.1. Computational design of doped SnO$_2$ catalysts

Ensuring the stability of catalysts is a crucial and challenging issue in exhaust aftertreatment systems, as it not only affects the catalyst's lifespan but also its cost [29]. The stability of the structure can be described by calculating the formation energy (E$_f$) of the catalyst, where E$_f$ < 0 indicates an exothermic synthesis process and a potentially successful synthesis, while E$_f$ > 0 eV indicates an unstable structure. To guarantee the structural stability of the catalyst, the formation energies of 45 kinds of doping models were calculated at temperatures ranging from 300 K to 1000 K, and the results are presented in Fig. 1. The most stable doping sites and their formation energies at 1000 K are listed in Table S1. Among them, 10 kinds of doping structures were found to be unstable, while the remaining 35 kinds of doping models exhibited exothermic synthesis, thus demonstrating stability even at a temperature of 1000 K.

The strength of interaction between reactants and the catalytic surface can be characterized by their adsorption energy [30]. In a specific reaction, both the adsorption energies of reactants and key intermediates play a simultaneous role in determining the activity and selectivity. If the adsorption energy is excessively strong, it can lead to surface poisoning and hinder the reaction rate. Conversely, if the adsorption energy is too weak, it results in a high energy barrier for the corresponding transition state, thus limiting the overall activity. Therefore, achieving excellent catalytic performance relies on optimizing the adsorption energies of crucial reaction intermediates [22, 31]. By adjusting the adsorption energies of essential active species, it becomes possible to steer the reaction towards the desired product and minimize undesired side reactions [32,33]. Furthermore, there is a strong correlation between the O p-band center and the oxygen exchange rate as well as the adsorption energy of important intermediates

[18,34]. Studies have shown that excellent catalytic performance is associated with an appropriate O p-band center, which is neither too close nor too far from the Fermi level [34,35]. Therefore, the adsorption energies of reactant NH$_3$ and key intermediate NH$_2$, along with the O p-band center, are used as catalytic performance descriptors to screen catalysts suitable for NH$_3$-SCO reaction.

The optimized adsorption structures of NH$_3$ and NH$_2$ are shown in Fig. S4-S8, and the preferred adsorption sites, corresponding adsorption energies, and O p-band centers are listed in Table S2. According to Table S2, a clear correlation is observed between the O p-band center and the adsorption energies of NH$_3$ and NH$_2$. Therefore, a correlation plot of the O p-band center and adsorption energies is constructed, with the O p-band center on the x-axis and the adsorption energies on the y-axis. As shown in Fig. 1(b), the adsorption energy of NH$_2$ is positively correlated with the O p-band center. When the O p-band center is less than − 2 eV, the adsorption energy of NH$_3$ shows a negative correlation with the O p-band center. Conversely, when the O p-band center is greater than − 2 eV, the adsorption energy of NH$_3$ exhibits a positive correlation. In the range of − 2 to − 2.2 eV, where the O p-band center is located, moderate adsorption energies for NH$_3$ and NH$_2$ are observed, with the O p-band center positioned in the middle. Therefore, it is suggested that doping SnO$_2$ with Ce, Ti, Zr, and Hf elements may lead to promising NH$_3$-SCO catalytic performance.

3.2. Experimental verification

3.2.1. Physical structure

The crystal structures of the synthesized doped SnO$_2$ samples were analyzed using XRD, as depicted in Fig. 2(a). In all cases, the samples displayed the tetragonal rutile structure characteristic of SnO$_2$ (PDF #99-0024). Compared to pure SnO$_2$, the diffraction peaks of the doped SnO$_2$ catalysts appeared broader, and no additional peaks were observed, indicating the successful doping of the metal M into the SnO$_2$ lattice, forming a solid solution. Fig. 2(b) presents the FTIR spectra recorded in the range of 500–1300 cm^{-1}. In the pure SnO$_2$ sample, the characteristic peak near 622 cm^{-1} arises from the vibrations of Sn-O-Sn and Sn-O bonds [36,37]. With the introduction of metal M doping, the peak shifted to higher wavenumbers, indicating the incorporation of M ions into the host lattice. No additional characteristic peaks were observed within the analyzed range, confirming that all M ions were fully incorporated into the SnO$_2$ lattice without the formation of additional pure-phase metal oxides, consistent with the XRD results. To validate the feasibility of the catalysts selected for the NH$_3$-SCO reaction through DFT calculations, two elements, Al (−1.57 eV) and Sb (−3.31 eV), were chosen at both ends of the O p-band center, and ASO
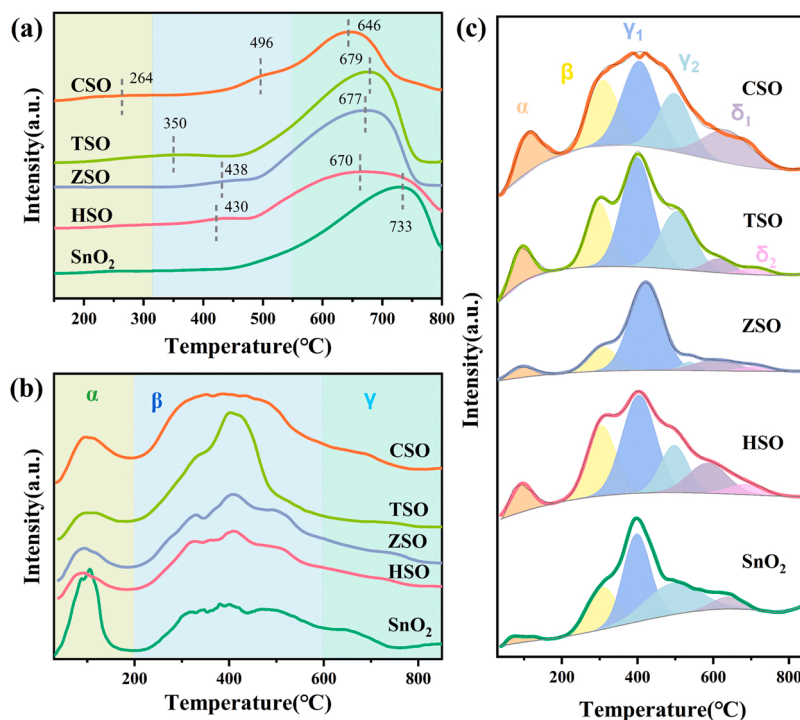
Fig. 3. (a) H₂-TPR, (b) NH₃-TPD, and (c) O₂-TPD of SnO₂ and doped SnO₂ catalysts.

and SSO catalysts were prepared using a co-precipitation method. The XRD results, as shown in Fig. S9, revealed that both ASO and SSO samples exhibited the tetragonal rutile structure, and no additional diffraction peaks were observed. The specific surface area and pore size information of the catalysts were determined through N₂ adsorption-desorption experiments, as shown in Fig. S10 and Table S3.

The doping of metal M promotes an increase in the specific surface area of the catalysts and a decrease in the average pore size. A larger specific surface area and smaller pore size facilitate the contact between the catalyst and reactants, thus favoring catalytic reactions [38,39].
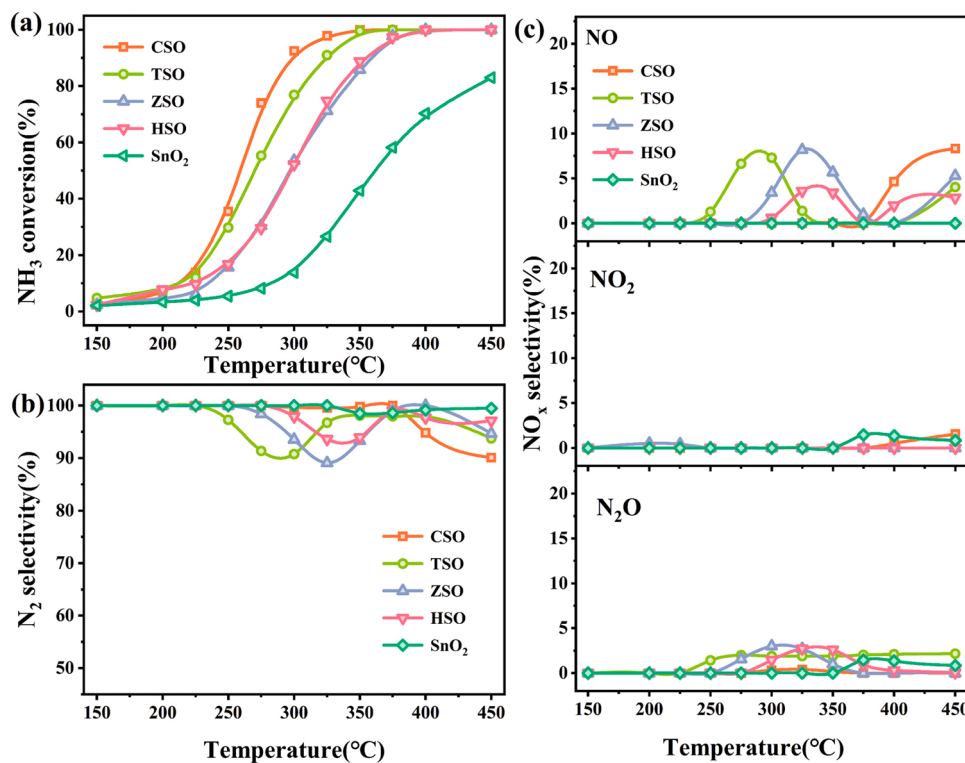

Fig. 4. (a) NH₃ conversion, (b) N₂ selectivity, and (c) NOₓ selectivity of SnO₂ and doped SnO₂ catalysts. Reaction conditions: 500 ppm NH₃ and 10 % O₂ in N₂ balance.
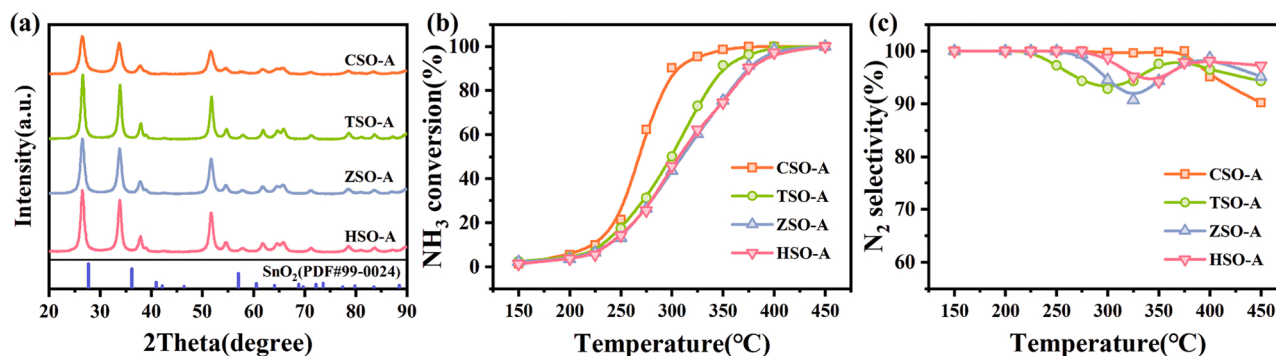
Fig. 5. (a) XRD patterns, (b) NH_3 conversion, and (c) N_2 selectivity of the catalysts after hydrothermal treatment. Reaction conditions: 500 ppm NH_3 and 10 % O_2 in N_2 balance.

3.2.2. Chemical properties

Fig. 3(a) illustrates the H_2-TPR results, and Table S4 presents the corresponding H_2 consumption values. On the SnO_2 catalyst, the reduction peak observed at around 430 °C can be attributed to the reduction of surface Sn^{4+}, whereas the reduction peak observed at around 733 °C is associated with the reduction of bulk Sn^{4+} and surface Sn^{2+} to Sn^0 [40,41]. On the doped SnO_2 catalysts, the reduction peaks between 300 and 500 °C are attributed to the reduction of surface Sn^{4+} and doped metal ions M^{4+}, while the reduction peaks between 600 and 700 °C are attributed to the reduction of bulk Sn^{4+} and surface Sn^{2+} to Sn^0. These reduction peaks shift to lower temperatures and the H_2 consumption increases. In the CSO sample, an additional reduction peak at 264 °C is observed, which is attributed to the reduction of Ce^{4+} and Sn^{4+} surface interactions in the catalyst [42]. This indicates that the doping of metal M promotes the redox performance of the catalyst, particularly in the case of CSO sample, where the interaction between Ce and Sn significantly enhances the redox properties.

Fig. 3(b) presents the NH_3-TPD results, and Table S5 provides the corresponding NH_3 desorption amounts. The NH_3 desorption peak observed below 200 °C can be attributed to physically adsorbed NH_3, whereas the NH_3 desorption peak within the 200–600 °C range is associated with NH_3 adsorbed on Brønsted or Lewis acid sites [7,13]. Notably, the introduction of metal M doping significantly enhances the adsorption of NH_3 on Brønsted or Lewis acid sites.

Fig. 3(c) presents the O_2-TPD results, while Table S6 provides the corresponding O_2 desorption amounts. The desorption peaks are labeled as α, β, γ, and δ, representing the desorption of physically adsorbed oxygen, chemically adsorbed oxygen, surface lattice oxygen, and bulk lattice oxygen, respectively. The results demonstrate that the introduction of metal M enhances the content of chemically adsorbed oxygen and surface lattice oxygen.

3.2.3. Catalytic activity

The NH_3-SCO catalytic performance is shown in Fig. 4, with significant enhancement in catalytic activity due to the doping of metal M, resulting in a T_{90} reduction of 125–175 °C. The N_2 selectivity remains above 90 % in the temperature range of 150–450 °C. Among them, the CSO sample exhibits the best catalytic performance, with a conversion rate exceeding 90 % at 300 °C and N_2 selectivity still above 90 % at 450 °C. Additionally, the NH_3-SCO catalytic performance of ASO and SSO samples was also tested, as shown in Fig. S11. Compared to SnO_2 samples, the catalytic activity slightly decreases with Sb doping, while the catalytic activity shows minimal improvement with Al doping. This indicates that the doping of Al or Sb does not significantly enhance the catalytic performance, consistent with the DFT calculation results. Therefore, the effective screening of target catalysts can be achieved by constructing activity descriptors. Due to the presence of a certain amount of water vapor in exhaust, the long-term water resistance of the CSO sample at 300 °C was tested, as shown in Fig. S12. Upon the addition of 5 % H_2O, a decline in catalytic activity was observed initially, with NH_3 conversion rate decreasing to 82 % within the first 30 min, followed by a stable performance. After 20 h, when H_2O was removed, the catalytic performance quickly recovered to 93 % within 10 min, and no byproducts were detected throughout the experiment. The decrease in catalytic activity induced by the introduction of H_2O can be attributed to the reversible competitive adsorption between H_2O and NH_3. As H_2O is removed, the active sites previously covered by H_2O gradually become exposed, thus restoring the catalytic performance [43]. Additionally, catalysts with a doping level of 20 % were synthesized. XRD results are presented in Fig. S13, and the outcomes of activity tests are shown in Fig. S14. The findings indicate that alterations in doping content exert limited influence on catalytic activity.

3.2.4. Catalyst stability

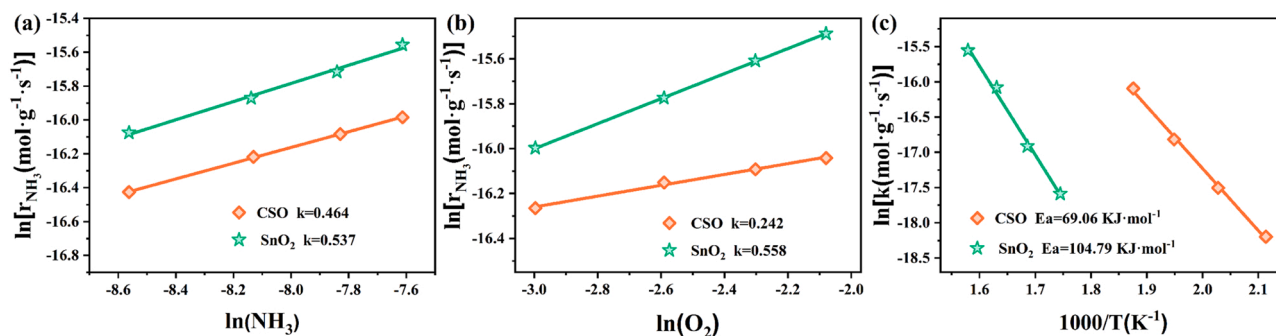The comparative analysis of catalysts' microstructure before and

Fig. 6. Kinetics of the reaction order for (a) NH_3, (b) O_2, and (c) the Arrhenius plot on CSO and SnO_2 samples. Reaction conditions: 200–500 ppm NH_3 and 5–12.5 % O_2 in N_2 balance.
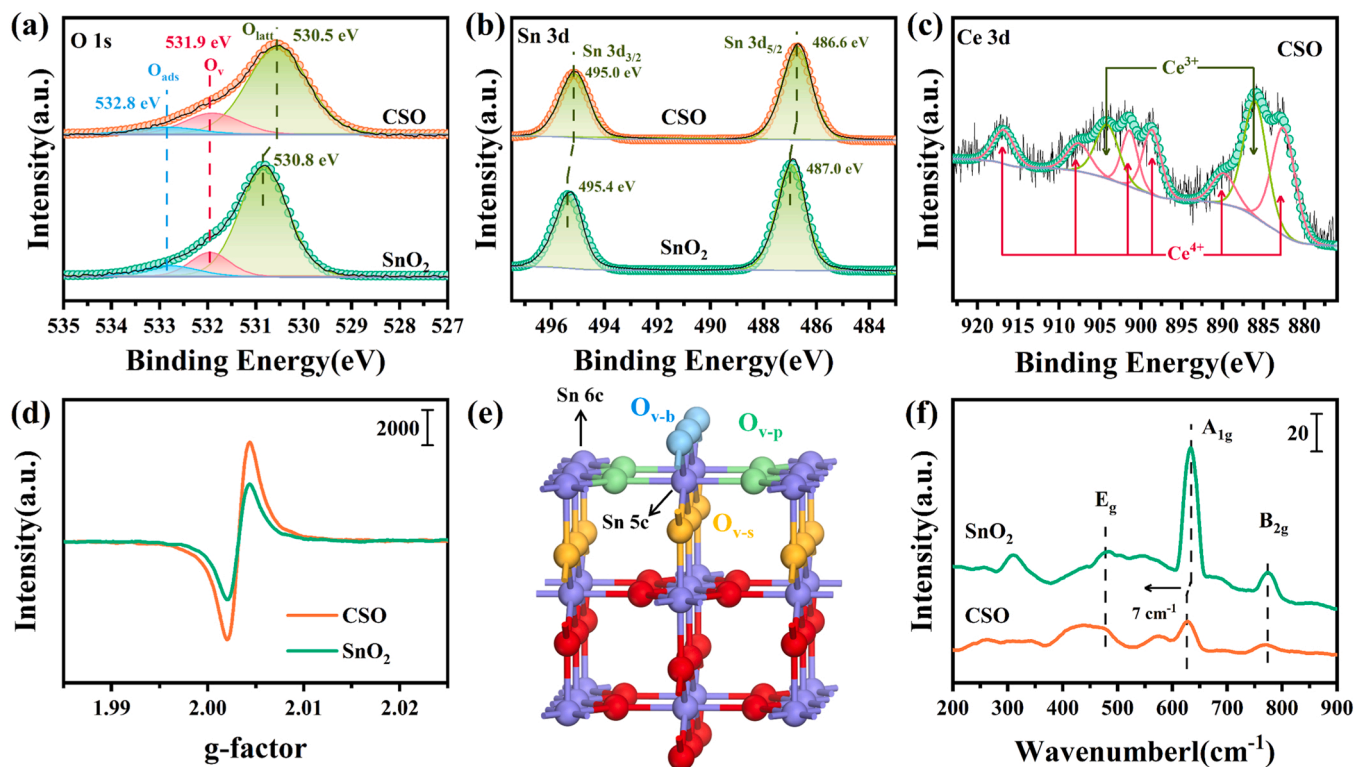
Fig. 7. (a) O 1s XPS spectra, (b) Sn 3d XPS spectra, (c) Ce 3d XPS spectra, (d) EPR spectra, (e) Oxygen vacancy types on the surface of SnO$_2$, and (f) Raman spectra. Sn, O, bridging oxygen, in-plane oxygen, and sub-bridging oxygen are shown in purple, red, blue, green, and orange, respectively.

after hydrothermal treatment is shown in Fig. S15. The fresh samples exhibit larger particle sizes, while after hydrothermal aging, some bulk structures are fragmented and reassemble into spherical aggregates. XRD patterns, as depicted in Fig. 5(a), indicate that all catalysts maintain the tetragonal rutile structure after hydrothermal treatment, without the appearance of new characteristic peaks, suggesting that the doped elements do not aggregate to form new oxides. This confirms the excellent structural stability of the catalysts selected through formation energy calculations. Therefore, by constructing stability descriptors, it is possible to effectively screen doped catalysts with superior structural stability. In addition, the NH$_3$-SCO catalytic performance of the catalysts before and after hydrothermal treatment was also tested, as shown in Fig. 5(b-c). The catalytic performance shows negligible changes after hydrothermal treatment, indicating their remarkable stability in terms of catalytic activity while maintaining structural stability.

3.3. Kinetic measurements

To further elucidate the intrinsic activity of the catalysts, CSO and SnO$_2$ samples were selected for kinetic studies. All kinetic experiments maintained NH$_3$ conversion rates below 15 % to avoid the influence of thermodynamic factors. The impact of gas flow rate on activity is shown in Fig. S16. To minimize the effects of external diffusion, a gas flow rate of 400 mL/min was chosen for the kinetic tests. Subsequently, the Weisz-Prater criterion (C$_{wp}$) [12,44,45] was calculated for the CSO and SnO$_2$ samples with an 60–80 mesh particle size. Table S7 presents all the computed results. The C$_{wp}$ values for both CSO and SnO$_2$ samples were found to be less than 0.3, indicating the absence of internal diffusion limitations under the current reaction conditions.

To analyze the interaction between reactants and catalysts, the reaction orders of NH$_3$ and O$_2$ were tested on CSO and SnO$_2$ samples, while considering the exclusion of internal and external diffusion effects, as shown in Fig. 6(a-b). SnO$_2$ exhibited higher reaction orders for both NH$_3$ and O$_2$, indicating more challenging adsorption and activation of

NH$_3$ and O$_2$ on the surface. The doping of Ce reduced the reaction order of O$_2$ from 0.588 to 0.242 on the CSO sample, suggesting that O$_2$ is more easily adsorbed and activated on CSO [13,46]. Evaluation of the Arrhenius curves and apparent activation energy further elucidated the intrinsic catalytic activity of the catalysts. As shown in Fig. 6(c), the apparent activation energy for SnO$_2$ (E$_a$ = 104.79 kJ/mol) was significantly higher than that for CSO (E$_a$ = 69.06 kJ/mol). Therefore, the doping of Ce likely facilitated the adsorption and activation of O$_2$, thereby reducing the reaction activation energy with NH$_3$. Furthermore, the impact of varying O$_2$ concentrations on the catalytic performance of the CSO sample was also investigated, as shown in Fig. S17. The catalytic activity increased with the elevation of O$_2$ concentration, further underscoring the significant role of O$_2$ adsorption and activation.

3.4. Oxygen vacancy

The XPS analysis results of CSO and SnO$_2$ samples are presented in Fig. 7(a–c) and Table S8. The O 1s spectrum in Fig. 7(a) can be fitted with three peaks. Peaks at binding energies of 530.5 and 530.8 eV are assigned to lattice oxygen (O$_{latt}$), while the peak at 531.9 eV is attributed to chemisorbed oxygen (O$_v$) captured by oxygen vacancies, and the peak at 532.8 eV is associated with chemisorbed surface oxygen (O$_{ads}$) [47–51]. Table S8 indicates that Ce doping primarily promotes an increase in chemisorbed oxygen captured by oxygen vacancies and a decrease in the proportion of lattice oxygen, suggesting an increase in the number of oxygen vacancies on the catalyst surface. Additionally, Ce doping leads to a reduction of 0.3 eV in the binding energy of lattice oxygen. According to the Pauling electronegativity scale [52], the lower electronegativity of Ce (1.12) compared to Sn (1.96) results in the bonding of oxygen atoms with Ce, leading to an increase in the electron density of the outermost valence electrons of oxygen, enhanced shielding effect, increased attractive force of the atomic nucleus, and subsequently, a decrease in the binding energy. Fig. 7(b) displays the XPS Sn 3d spectrum, where the peaks in the range of 486.6–487.0 eV and
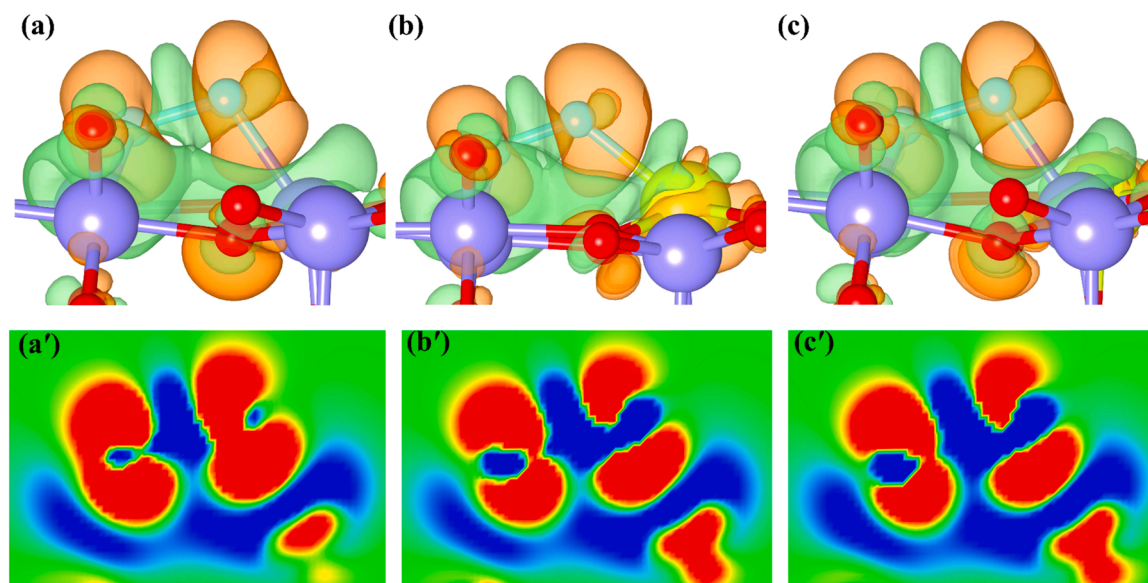
Fig. 8. Charge density differences of O_2 adsorption on (a) SnO_2-O_v, (b) CSO-O_v-1, and (c) CSO-O_v-2 models. (a′-c′) Corresponding contour plots. Sn, Ce, O, and adsorbed O_2 molecule are shown in purple, yellow, red, and turquoise, respectively. In panels (a–c), the orange-red area represents a positive charge, while the light green area represents a negative charge. In panels (a′-c′), the red, green, and blue colors indicate the magnitude of electron density, corresponding to 0.003, 0, and − 0.003 eV, respectively.

495.0–495.4 eV represent the spin-orbit splitting of Sn^{4+}, indicating the absence of low-valence Sn species on the catalyst surface [42,53]. After Ce doping, the binding energy of Sn^{4+} shifts towards lower energy by 0.6 eV, indicating an electron-rich state of Sn resulting from the formation of oxygen vacancies. During the formation of oxygen vacancies, the two electrons carried by oxygen are bound to the vacancies, leaving the remaining two electrons unable to exist stably within the vacancies and transferring to the surrounding metal cations, causing the metal cations to be in an electron-rich state [54,55]. Therefore, with Ce doping, the concentration of oxygen vacancies increases, leading to a decrease in the binding energy of Sn. Fig. 7(c) presents the Ce 3d XPS spectrum, which showcases eight components corresponding to the Ce^{4+} and Ce^{3+} species [56,57]. Furthermore, Table S8 indicates that the catalyst surface contains approximately 9.12 % of Ce element, which is close to the proportion during catalyst synthesis, confirming the uniform doping of Ce.

The EPR spectra of CSO and SnO_2 samples are shown in Fig. 7(d). The signal at g = 2.03 is attributed to electron capture on oxygen vacancies. The CSO sample exhibits a stronger signal, indicating a higher concentration of oxygen vacancies [58]. This is consistent with the XPS analysis results, where Ce doping leads to an increase in the concentration of oxygen vacancies, which may be an important factor promoting O_2 adsorption and activation.

In general, the SnO_2 surface primarily exhibits three types of oxygen vacancies, as shown in Fig. 7(e). Oxygen atoms connected to Sn 5c are referred to as bridging oxygen (blue), and their absence leads to the formation of surface bridging oxygen vacancies (O_{v-b}). Oxygen atoms connected to both Sn 5c and Sn 6c are known as in-plane oxygen (green), and their vacancies are referred to as in-plane oxygen vacancies (O_{v-p}). Oxygen atoms in the subsurface region are termed sub-bridging oxygen (orange), and their vacancies are called sub-bridging oxygen vacancies (O_{v-s}) [59]. Raman spectroscopy was performed to further elucidate the types of oxygen vacancies on the CSO sample, as depicted in Fig. 7(f). Peaks observed at 477 cm^{-1}, 633 cm^{-1}, and 774 cm^{-1} in the Raman spectra of SnO_2 correspond to the vibrational modes of E_g, A_{1g}, and B_{2g}, respectively [59–61]. With Ce doping, the intensities of the A_{1g} and B_{2g} peaks decrease, and the A_{1g} peak experiences a redshift of 7 cm^{-1}, which can be attributed to an increased presence of surface bridging oxygen vacancies (O_{v-b}) [59–63].

3.5. Activation of oxygen

The kinetic analysis indicates that the doping of Ce primarily promotes the adsorption and activation of O_2, thereby enhancing the NH_3-SCO performance. XPS, EPR, and Raman spectroscopy confirm that Ce doping leads to an increase in the concentration of oxygen vacancies on the catalyst surface, with surface bridging oxygen vacancies being the dominant type of newly formed vacancies. Therefore, we hypothesize that Ce doping increases the concentration of surface bridging oxygen vacancies, which in turn activate O_2 at these sites, ultimately leading to the improvement of NH_3-SCO performance. To validate this hypothesis, the activation mechanism of O_2 at surface bridging oxygen vacancies was computationally investigated.

The HR-TEM images in Fig. S18 illustrate the predominant exposure of the (110) surface of both SnO_2 and CSO catalysts. Additionally, the SnO_2(110) surface is characterized by high thermodynamic stability and has been extensively studied both experimentally and theoretically, making it a suitable choice as the adsorption surface [64–67]. In the SnO_2 model, one bridging oxygen was removed from the surface to simulate the presence of an oxygen vacancy, denoted as SnO_2-O_v. In the CSO model, two types of surface bridging oxygen (near and far from Ce atoms) were removed to simulate oxygen vacancies, named CSO-O_v-1 and CSO-O_v-2, respectively. The optimized geometries are shown in Fig. S19. Ce doping reduces the formation energy of oxygen vacancies from 1.95 eV to 1.57 eV and 1.41 eV, facilitating the involvement of lattice oxygen in reactions. Fig. S20 displays the adsorption configurations and energies of O_2 on the SnO_2-O_v, CSO-O_v-1, and CSO-O_v-2 models. O_2 prefers to bridge between oxygen vacancies and Sn 5c (or Ce 5c) sites. As a nonpolar molecule, O_2 possesses two pairs of unpaired electrons, requiring external electron pairing for its oxygen atoms. The formation of oxygen vacancies induces a locally electron-rich environment around the neighboring metal cations, allowing for more electron transfer to O_2 and pairing with its unpaired oxygen electrons. Consequently, O_2 has a higher affinity for adsorption on oxygen vacancies. Unexpectedly, O_2 exhibits stronger adsorption on SnO_2, but excessive O_2 adsorption can result in overly stable adsorption, hindering the breaking of O-O bonds.

Bader charge calculations reveal that the SnO_2-O_v, CSO-O_v-1, and CSO-O_v-2 models transfer 1.05, 1.11, and 1.17 |e|, respectively, to the
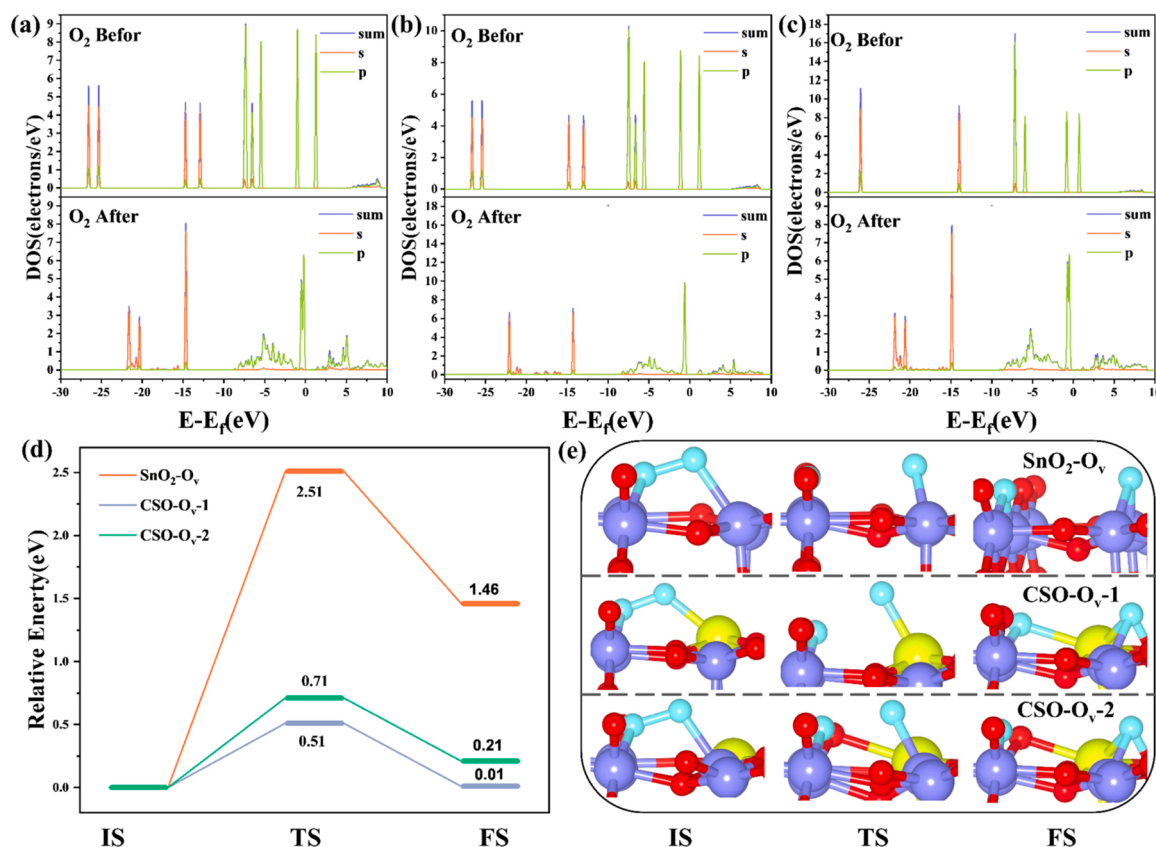
Fig. 9. Partial density of states (PDOS) of O_2 before and after adsorption on (a)SnO_2, (b) CSO-O_v-1, and (c) CSO-O_v-2. (d) dissociation energy barrier and (e) optimized structural models of O_2 on various catalysts. Sn, Ce, O, and adsorbed O_2 molecule are shown in purple, yellow, red, and turquoise, respectively. IS, TS, and FS represent the initial state, transition state, and final state, respectively.

adsorbed O_2, indicating the activation of adsorbed O_2 molecules into superoxide ions (O^{2-}) on the catalyst surface. Ce doping facilitates charge transfer, thereby enhancing O_2 activation. Subsequently, the difference charge density before and after O_2 adsorption was calculated, as shown in Fig. 8(a–c). The adsorbed O_2 accepts electrons from the support, primarily accumulating on the O atom. In order to directly visualize the alterations in electron density surrounding the adsorbed O_2, the modifications in charge density within the Sn 6c-O-O-Sn 5c (or Sn 6c-O-O-Ce 5c) plane were extracted from the three-dimensional plots, as illustrated in Fig. 8(a'–c'). From the figures, it is evident that Ce doping leads to a decrease in the charge density between the two oxygen atoms, weakening the O-O bond and facilitating its cleavage.

The density of states (DOS) plots before and after O_2 adsorption on different models are shown in Fig. 9(a–c). By comparing with the molecular orbital energy level diagram of O_2 (Fig. S21), it can be observed that the first peak below the Fermi level (HOMO) corresponds to the degenerate π * antibonding orbitals of π_{2Px*} and π_{2Py*}, while the first peak above the Fermi level (LUMO) corresponds to the σ * antibonding orbital of σ_{2Pz*}. As O_2 approaches the catalyst surface, electrons from the catalyst metal are injected into the σ * antibonding orbital of O_2, causing the splitting of the σ * antibonding orbital and the formation of new bonding and antibonding orbitals, indicating further activation of O_2. Ce doping leads to more pronounced shifts of the newly formed bonding and antibonding orbitals towards higher and lower energies, especially in the CSO-1 model, suggesting that Ce doping enhances the interaction between O_2 and the surface, facilitating O_2 activation. Moreover, the dissociation energy barriers of O_2 on different catalyst surfaces also confirm that Ce doping promotes O-O bond cleavage, as shown in Fig. 9 (c-d). O_2 is more likely to dissociate on CSO-O_v-1 with a dissociation energy barrier of 0.51 eV, much lower than the dissociation energy barrier of O_2 on SnO_2-O_v (2.51 eV). Meanwhile, the additional low-
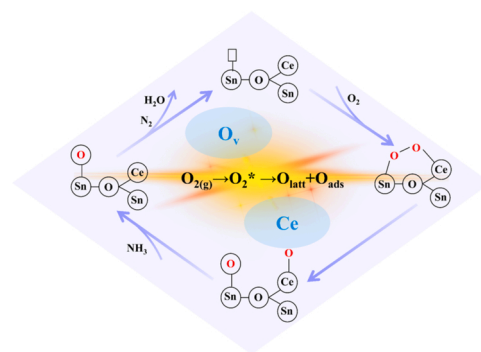
temperature reduction peaks in the H_2-TPR spectra of the CSO samples are also related, further suggesting that the Ce reference promotes the activation of O_2.

In conclusion, the synergy between oxygen vacancies and Ce doping facilitates the activation of O_2. Gaseous O_2 initially adsorbs on the oxygen vacancies and Ce atoms. Subsequently, the O-O bond breaks, leading to the formation of activated adsorbed oxygen species and active lattice oxygen species. Finally, they react with NH_3 or intermediates, resulting in the consumption and formation of a catalyst surface rich in oxygen vacancies. The detailed process of O_2 activation is illustrated in Fig. 10.

Fig. 10. Mechanism of O_2 activation.

3.6. NH$_3$-SCO reaction mechanism

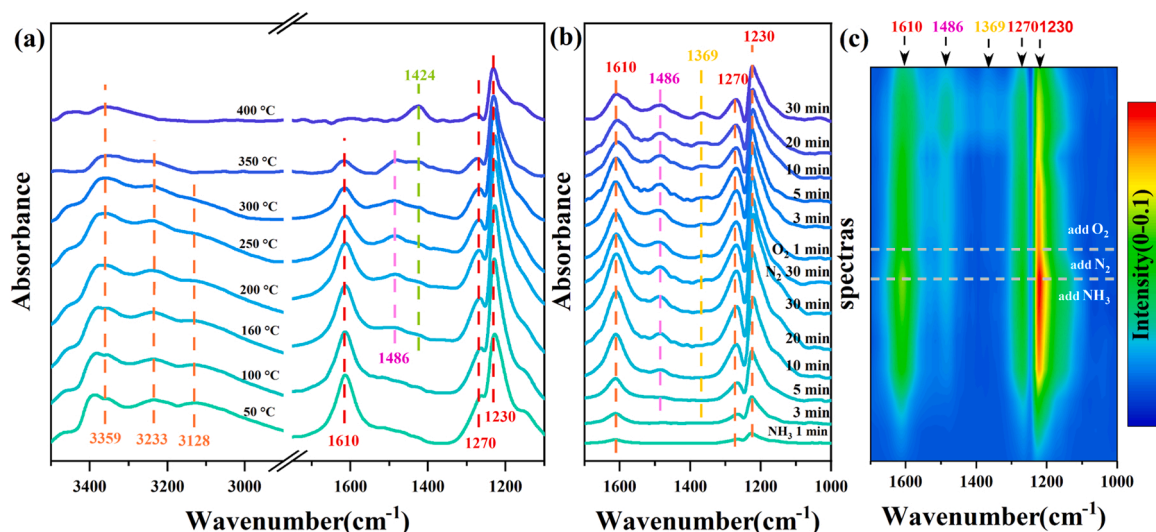In situ DRIFTS spectra were recorded to further investigate the NH$_3$-

Fig. 11. (a) Steady state in situ DRIFTS under reaction conditions, (b) in situ DRIFTS of reaction between adsorbed NH_3 and O_2, and (c) the mapping results of in situ DRIFTS of reaction between adsorbed NH_3 and O_2. The Lewis acid sites, N-H stretching vibrations of coordinated NH_3, $-NH_2$, HNO, and nitrite species are shown in red, orange-red, light pink, magenta, and green, respectively.

SCO reaction mechanism on the CSO sample over the temperature range of 50–400 °C, as shown in Fig. 11(a). At 50 °C, characteristic peaks of Lewis acid sites (1610 cm^{-1}, 1270 cm^{-1}, and 1230 cm^{-1}) [13,68–70] and coordinated NH_3 (3359 cm^{-1}, 3233 cm^{-1}, and 3128 cm^{-1}) [69,71] were observed, and the intensity of the NH_3 adsorption peaks gradually weakened with increasing temperature. At 160 °C, the appearance of the HNO species (1486 cm^{-1}) [13,68,72] was observed, and its peak intensity initially increased and then decreased with temperature, reaching its maximum at 250 °C, indicating the significance of the HNO species as an important intermediate in the NH_3-SCO process. At 250 °C, the presence of trans-nitrous acid (1424 cm^{-1}) [73] was observed, and the peak intensity gradually increased with temperature.

The transient reactions at 250 °C are shown in Fig. 11(b). After 1 min of NH_3 introduction, characteristic peaks of Lewis acid sites (1610 cm^{-1}, 1270 cm^{-1}, and 1230 cm^{-1}) [13,68–70] were observed, and their intensities increased with increasing NH_3 exposure time. After 5 min of NH_3 introduction, the appearance of the HNO species (1486 cm^{-1}) [13,68,72] was observed, and its intensity increased with time, indicating the involvement of surface lattice oxygen in the reaction. After 1 min of O_2 introduction, the $-NH_2$ species (1369 cm^{-1}) [69] was observed. To better visualize the changes in peak intensities, they were mapped onto a two-dimensional space, as shown in Fig. 11(c). During NH_3 introduction, a clear enhancement of the Lewis acid site adsorption peaks was observed, while after O_2 introduction, the intensity of the Lewis acid site adsorption peaks decreased, and the intensities of the $-NH_2$ and HNO species peaks increased.

In conclusion, considering the formation of HNO species and nitrite species, we propose that the NH_3-SCO reaction on the CSO sample follows both the internal selective catalytic reduction (i-SCR) mechanism and the imide (-NH) mechanism. The -NH mechanism predominates in the low-temperature range, while the i-SCR mechanism dominates in the high-temperature range.

4. Conclusions

In this study, we have systematically developed a DFT-based screening method for selective catalytic oxidation of ammonia using Sn-based catalysts, aiming to reduce repetitive trial-and-error experiments. The correlation between DFT-driven descriptors and experimental results has demonstrated the feasibility of the screening approach. Furthermore, the promoting mechanism of Ce element doping on the NH_3-SCO reaction has been further elucidated, providing a

direction for exploring new-generation DFT descriptors for selective oxidation of NH_3. In conclusion, this work presents a viable pathway to screen Sn-based catalysts for the NH_3-SCO reaction from the perspective of DFT calculations, avoiding repetitive trial-and-error experiments and offering new design strategies for developing long-lasting and highly active catalysts for ammonia removal.

CRediT authorship contribution statement

Yan Zhang: Writing – original draft, DFT calculations, Investigation, Formal analysis, Methodology. **Min Zhang:** Writing – original draft, Investigation, Data curation. **Meng Wang:** Investigation, Data curation, Validation. **Caixia Liu:** Supervision, Conceptualization, Project administration, Funding acquisition, Writing – review & editing. **Qingling Liu:** Supervision, Project administration. **Weichao Wang:** Supervision, Conceptualization. **Ziyin Zhang:** Supervision, Funding acquisition. **Rui Han:** Supervision. **Na Ji:** Supervision. All authors discussed and commented on the manuscript.

Declaration of Competing Interest

The authors declare that they have no known competing financial interests or personal relationships that could have appeared to influence the work reported in this paper.

Data Availability

Data will be made available on request.

Acknowledgements

Data Availability

Data will be made available on request.

Appendix A. Supporting information

Supplementary data associated with this article can be found in the online version at doi:10.1016/j.apcatb.2023.123256.

References

[1] M.-C. Chiong, C.T. Chong, J.-H. Ng, S. Mashruk, W.W.F. Chong, N.A. Samiran, G. R. Mong, A. Valera-Medina, Advancements of combustion technologies in the ammonia-fuelled engines, Energy Convers. Manag. 244 (2021).

[2] E. Nadimi, G. Przybyla, D. Emberson, T. Lovas, L. Ziolkowski, W. Adamczyk, Effects of using ammonia as a primary fuel on engine performance and emissions in an ammonia/biodiesel dual-fuel CI engine, Int. J. Energy Res. 46 (2022) 15347–15361.

[3] J. Shin, S. Park, Numerical analysis for optimizing combustion strategy in an ammonia-diesel dual-fuel engine, Energy Convers. Manag. 284 (2023).

[4] C. Kurien, P.S. Varma, M. Mittal, Effect of ammonia energy fractions on combustion stability and engine characteristics of gaseous (ammonia/methane) fuelled spark ignition engine, Int. J. Hydrogen Energy 48 (2023) 1391–1400.

[5] C. Kurien, M. Mittal, Review on the production and utilization of green ammonia as an alternate fuel in dual-fuel compression ignition engines, Energy Convers. Manag. 251 (2022).

[6] S. Jin, B. Wu, Z. Zi, P. Yang, T. Shi, J. Zhang, Effects of fuel injection strategy and ammonia energy ratio on combustion and emissions of ammonia-diesel dual-fuel engine, Fuel 341 (2023).

[7] Y.J. Chen, X. Chen, X.Y. Ma, Y.T. Tang, Y.K. Zhao, A.M. Zhang, C. Wang, C. Du, B. Shan, Selective catalytic oxidation of ammonia over AMn$_2$O$_5$(A=Sm,Y,Gd) and reaction selectivity promotion through Nb decoration, J. Catal. 402 (2021) 10–21.

[8] J. Peng, S. Chen, H. Lu, Y. Liu, J. Wu, Spatiotemporal patterns of remotely sensed PM2.5 concentration in China from 1999 to 2011, Remote Sens. Environ. 174 (2016) 109–121.

[9] A. Scheuer, W. Hauptmann, A. Drochner, J. Gieshoff, H. Vogel, M. Votsmeier, Dual layer automotive ammonia oxidation catalysts: experiments and computer simulation, Appl. Catal. B-Environ. 111 (2012) 445–455.

[10] M. Jablonska, Progress on selective catalytic ammonia oxidation (NH$_3$-SCO) over Cu-containing zeolite-based catalysts, Chemcatchem 12 (2020) 4490–4500.

[11] H. Sun, Z. Qu, Progress in selective catalytic oxidation of ammonia to nitrogen, Chin. Sci. Bull. -Chin. 65 (2020) 2835–2852.

[12] H. Wang, M. Lin, T. Murayama, S. Feng, M. Haruta, H. Miura, T. Shishido, Ag size/ structure-dependent effect on low-temperature selective catalytic oxidation of NH$_3$ over Ag/MnO$_2$, ACS Catalysis 11 (2021) 8576–8584.

[13] F. Wang, J. Ma, G. He, M. Chen, C. Zhang, H. He, Nanosize effect of Al$_2$O$_3$ in Ag/ Al$_2$O$_3$ catalyst for the selective catalytic oxidation of ammonia, ACS Catal. 8 (2018) 2670–2682.

[14] S. Ge, X. Liu, J. Liu, H. Liu, H. Liu, X. Chen, G. Wang, J. Chen, G. Zhang, Y. Zhang, J. Li, Synthesis of Ti$_x$Sn$_{1-x}$O$_2$ mixed metal oxide for copper catalysts as high-efficiency NH$_3$ selective catalytic oxidation, Fuel 314 (2022), 123061.

[15] R. Ma, Y. Du, X. Liu, J. Liu, X. Wu, Synthesis of a novel CoNiV mixed oxides from hydrotalcite precursor and its application for selective catalytic oxidation of slip ammonia, J. Energy Inst. 102 (2022) 327–336.

[16] Y. Zhang, M. Zhang, Y. Zang, H. Wang, C. Liu, L. Wei, Y. Wang, L. He, W. Wang, Z. Zhang, R. Han, N. Ji, C. Song, X. Lu, D. Ma, Y. Sun, Q. Liu, Elimination of NH3 by interfacial charge transfer over the Ag/ CeSnOX tandem catalyst, ACS Catal. (2023) 1449–1461.

[17] L. Zhang, C. Zhang, H. He, The role of silver species on Ag/Al2O3 catalysts for the selective catalytic oxidation of ammonia to nitrogen, J. Catal. 261 (2009) 101–109.

[18] Z.-J. Zhao, S. Liu, S. Zha, D. Cheng, F. Studt, G. Henkelman, J. Gong, Theory-guided design of catalytic materials using scaling relationships and reactivity descriptors, Nat. rev Mater. 4 (2019) 792–804.

[19] X. Chang, Z.-J. Zhao, Z. Lu, S. Chen, R. Luo, S. Zha, L. Li, G. Sun, C. Pei, J. Gong, Designing single-site alloy catalysts using a degree-of-isolation descriptor, Nat. Nanotechnol. (2023).

[20] X. Lin, Y. Wang, X. Chang, S. Zhen, Z.-J. Zhao, J. Gong, High-throughput screening of electrocatalysts for nitrogen reduction reactions accelerated by interpretable intrinsic descriptor, Angew. Chem. -Int. Ed. (2023).

[21] A.B. Laursen, A.S. Varela, F. Dionigi, H. Fanchiu, C. Miller, O.L. Trinhammer, J. Rossmeisl, S. Dahl, Electrochemical hydrogen evolution: Sabatier's principle and the volcano plot, J. Chem. Educ. 89 (2012) 1595–1599.

[22] A.J. Medford, A. Vojvodic, J.S. Hummelshøj, J. Voss, F. Abild-Pedersen, F. Studt, T. Bligaard, A. Nilsson, J.K. Nørskov, From the Sabatier principle to a predictive theory of transition-metal heterogeneous catalysis, J. Catal. 328 (2015) 36–42.

[23] S. Jiao, X. Fu, H. Huang, Descriptors for the evaluation of electrocatalytic reactions: d-band theory and beyond, Adv. Funct. Mater. 32 (2022).

[24] A. Grimaud, K.J. May, C.E. Carlton, Y.-L. Lee, M. Risch, W.T. Hong, J. Zhou, Y. Shao-Horn, Double perovskites as a family of highly active catalysts for oxygen evolution in alkaline solution, Nat. Commun. 4 (2013).

[25] J. Greeley, T.F. Jaramillo, J. Bonde, I.B. Chorkendorff, J.K. Norskov, Computational high-throughput screening of electrocatalytic materials for hydrogen evolution, Nat. Mater. 5 (2006) 909–913.

[26] E.R. Cave, C. Shi, K.P. Kuhl, T. Hatsukade, D.N. Abram, C. Hahn, K. Chan, T. F. Jaramillo, Trends in the catalytic activity of hydrogen evolution during CO$_2$ electroreduction on transition metals, ACS Catalysis 8 (2018) 3035–3040.

[27] G. Kresse, J. Furthmuller, Efficient iterative schemes for ab initio total-energy calculations using a plane-wave basis set, Phys. Rev. B 54 (1996) 11169–11186.

[28] G. Kresse, J. Furthmuller, Efficiency of ab-initio total energy calculations for metals and semiconductors using a plane-wave basis set, Comput. Mater. Sci. 6 (1996) 15–50.

[29] M.J. Hazlett, W.S. Epling, Heterogeneous catalyst design: zoned and layered catalysts in diesel vehicle aftertreatment monolith reactors, Can. J. Chem. Eng. 97 (2019) 188–206.

[30] J.K. Norskov, T. Bligaard, B. Hvolbaek, F. Abild-Pedersen, I. Chorkendorff, C. H. Christensen, The nature of the active site in heterogeneous metal catalysis, Chem. Soc. Rev. 37 (2008) 2163–2171.

[31] A.B. Laursen, A.S. Varela, F. Dionigi, H. Fanchiu, C. Miller, O.L. Trinhammer, J. Rossmeisl, S. Dahl, Electrochemical hydrogen evolution: sabatier's principle and the volcano plot, J. Chem. Educ. 89 (2012) 1595–1599.

[32] B. Huang, H. Kobayashi, T. Yamamoto, T. Toriyama, S. Matsumura, Y. Nishida, K. Sato, K. Nagaoka, M. Haneda, W. Xie, Y. Nanba, M. Koyama, F. Wang, S. Kawaguchi, Y. Kubota, H. Kitagawa, A.C.O. Adsorption, Site change induced by copper substitution in a ruthenium catalyst for enhanced CO oxidation activity, Angew. Chem. Int Ed. Engl. 58 (2019) 2230–2235.

[33] S. Kattel, P.J. Ramírez, J.G. Chen, J.A. Rodriguez, P. Liu, Active sites for CO$_2$ hydrogenation to methanol on Cu/ZnO catalysts, Science 355 (2017) 1296–1299.

[34] Y.-L. Lee, J. Kleis, J. Rossmeisl, S.-H. Yang, M. Dane, Prediction of solid oxidefuel cell cathode activity with first-principles descriptors, Energy Environ. Sci. 4 (2011) 3966–3970.

[35] A. Grimaud, K.J. May, C.E. Carlton, Y.L. Lee, M. Risch, W.T. Hong, J. Zhou, Y. Shao-Horn, Double perovskites as a family of highly active catalysts for oxygen evolution in alkaline solution, Nat. Commun. 4 (2013) 2439.

[36] Y. Liu, F. Yang, X. Yang, Size-controlled synthesis and characterization of quantum-size SnO$_2$ nanocrystallites by a solvothermal route, Colloids Surf. A-Physicochem. Eng. Asp. 312 (2008) 219–225.

[37] V.S. Jahnavi, S.K. Tripathy, A.V.N.R. Rao, Structural, optical, magnetic and dielectric studies of SnO$_2$ nano particles in real time applications, Phys. B-Condens. Matter 565 (2019) 61–72.

[38] F. Gao, X. Tang, H. Yi, S. Zhao, J. Wang, T. Gu, Improvement of activity, selectivity and H$_2$O&SO$_2$-tolerance of micro-mesoporous CrMn$_2$O$_4$ spinel catalyst for low-temperature NH$_3$-SCR of NO$_x$, Appl. Surf. Sci. 466 (2019) 411–424.

[39] Z. Liu, Y. Yi, S. Zhang, T. Zhu, J. Zhu, J. Wang, Selective catalytic reduction of NO$_x$ with NH$_3$ over Mn-Ce mixed oxide catalyst at low temperatures, Catal. Today 216 (2013) 76–81.

[40] C. Liu, H. Xian, Z. Jiang, L. Wang, J. Zhang, L. Zheng, Y. Tan, X. Li, Insight into the improvement effect of the Ce doping into the SnO$_2$ catalyst for the catalytic combustion of methane, Appl. Catal. B-Environ. 176 (2015) 542–552.

[41] C. Santra, M. Pramanik, K.K. Bando, S. Maity, B. Chowdhury, Gold nanoparticles on mesoporous Cerium-Tin mixed oxide for aerobic oxidation of benzyl alcohol, J. Mol. Catal. A-Chem. 418 (2016) 41–53.

[42] Z. Liu, X. Feng, Z. Zhou, Y. Feng, J. Li, Ce-Sn binary oxide catalyst for the selective catalytic reduction of NO$_x$ by NH$_3$, Appl. Surf. Sci. 428 (2018) 526–533.

[43] F. Wang, Y. Zhu, Z. Li, Y. Shan, W. Shan, X. Shi, Y. Yu, C. Zhang, K. Li, P. Ning, Y. Zhang, H. He, Promoting effect of acid sites on NH$_3$-SCO activity with water vapor participation for Pt-Fe/ZSM-5 catalyst, Catal. Today 376 (2021) 311–317.

[44] M.A. Vannice, Kinetics of Catalytic Reactions, Springer Scienceþbusiness Media, Inc., New York, 2005.

[45] H.S. Fogler, Elements of Chemical Reaction Engineering, Pearson Education, Inc, 2005.

[46] T. Lan, J. Deng, X. Zhang, F. Wang, X. Liu, D. Cheng, D. Zhang, Unraveling the promotion effects of dynamically constructed CuO$_x$-OH interfacial sites in the selective catalytic oxidation of ammonia, ACS Catalysis 12 (2022) 3955–3964.

[47] J.H. Shin, G.J. Kim, S.C. Hong, Reaction properties of ruthenium over Ru/TiO$_2$ for selective catalytic oxidation of ammonia to nitrogen, Appl. Surf. Sci. 506 (2020), 144906.

[48] M. Zhang, J. Zhang, Z. Zhou, Q. Zhang, Y. Tan, Y. Han, Effects of calcination atmosphere on the performance of the co-precipitated Ni/ZrO$_2$ catalyst in dry reforming of methane, Can. J. Chem. Eng. 100 (2022) 172–183.

[49] Z. Kang, E. Lin, N. Qin, J. Wu, B. Yuan, D. Bao, Effect of oxygen vacancies and crystal symmetry on piezocatalytic properties of Bi$_2$WO$_6$ ferroelectric nanosheets for wastewater decontamination, Environ. Sci.: Nano 8 (2021) 1376–1388.

[50] M. Sun, S. Wang, Y. Li, H. Xu, Y. Chen, Promotion of catalytic performance by adding W into Pt/ZrO$_2$ catalyst for selective catalytic oxidation of ammonia, Appl. Surf. Sci. 402 (2017) 323–329.

[51] Y. Wang, H. Chang, C. Shi, L. Duan, J. Li, G. Zhang, L. Guo, Y. You, Novel Fe-Ce-O mixed metal oxides catalyst prepared by hydrothermal method for Hg^0 oxidation in the presence of NH$_3$, Catal. Commun. 100 (2017) 210–213.

[52] E.A.K. James, E. Huheey, L. Richard, Keiter. Inorganic Chemistry: Principles of Structure and Reactivity, 4th ed., HarperCollins College Publishers, New York, 1993.

[53] X. Xu, Y. Tong, J. Zhang, X. Fang, J. Xu, F. Liu, J. Liu, W. Zhong, O.E. Lebedeva, X. Wang, Investigation of lattice capacity effect on Cu^{2+}-doped SnO$_2$ solid solution catalysts to promote reaction performance toward NO$_x$-SCR with NH$_3$, Chin. J. Catal. 41 (2020) 877–888.

[54] H.A. Tahini, X. Tan, U. Schwingenschlogl, S.C. Smith, Formation and migration of oxygen vacancies in SrCoO$_3$ and their effect on oxygen evolution reactions, ACS Catal. 6 (2016) 5565–5570.

[55] J. Paier, C. Penschke, J. Sauer, Oxygen defects and surface chemistry of ceria: quantum chemical studies compared to experiment, Chem. Rev. 113 (2013) 3949–3985.

[56] S.M. Lee, H.H. Lee, S.C. Hong, Influence of calcination temperature on Ce/TiO$_2$ catalysis of selective catalytic oxidation of NH$_3$ to N$_2$, Appl. Catal. A-Gen. 470 (2014) 189–198.

[57] Z. Wang, Z. Qu, X. Quan, Z. Li, H. Wang, R. Fan, Selective catalytic oxidation of ammonia to nitrogen over CuO-CeO$_2$ mixed oxides prepared by surfactant-templated method, Appl. Catal. B-Environ. 134 (2013) 153–166.

[58] Q. Zeng, Y. Cui, L. Zhu, Y. Yao, Increasing oxygen vacancies at room temperature in SnO$_2$ for enhancing ethanol gas sensing, Mater. Sci. Semicond. Process. 111 (2020), 104962.

[59] M. Kaur, N.S. Ramgir, U.K. Gautam, S.K. Ganapathi, S. Bhattacharya, N. Datta, V. Saxena, A.K. Debnath, D.K. Aswal, S.K. Gupta, H$_2$S sensors based on SnO$_2$ films: RGTO verses RF sputtering, Mater. Chem. Phys. 147 (2014) 707–714.

[60] W.B.H. Othmen, B. Sieber, H. Elhouichet, A. Addad, B. Gelloz, M. Moreau, S. Szunerits, R. Boukherroub, Effect of high Fe doping on Raman modes and optical properties of hydrothermally prepared SnO$_2$ nanoparticles, Mater. Sci. Semicond. Process. 77 (2018) 31–39.

[61] X. Wang, X. Wang, Q. Di, H. Zhao, B. Liang, J. Yang, Mutual effects of fluorine dopant and oxygen vacancies on structural and luminescence characteristics of F doped SnO$_2$ nanoparticles, Materials 10 (2017) 1398.

[62] L.Z. Liu, T.H. Li, X.L. Wu, J.C. Shen, P.K. Chu, Identification of oxygen vacancy types from Raman spectra of SnO$_2$ nanocrystals, J. Raman Spectrosc. 43 (2012) 1423–1426.

[63] M. Epifani, J.D. Prades, E. Comini, E. Pellicer, M. Avella, P. Siciliano, G. Faglia, A. Cirera, R. Scotti, F. Morazzoni, J.R. Morante, The role of surface oxygen vacancies in the NO$_2$ sensing properties of SnO$_2$ nanocrystals, J. Phys. Chem. C 112 (2008) 19540–19546.

[64] Y. Sun, S. Sun, Y. Zheng, Z. Zhang, T. Hou, H. Du, J. Wang, The role of oxygen vacancies on SnO$_2$ in improving formaldehyde competitive adsorption: a DFT study with an experimental verification, Appl. Surf. Sci. 570 (2021), 151110.

[65] D. Wang, Y. Chen, Z. Liu, L. Li, C. Shi, H. Qin, J. Hu, CO$_2$-sensing properties and mechanism of nano-SnO$_2$ thick-film sensor, Sens. Actuators B-Chem. 227 (2016) 73–84.

[66] Y. Chen, X. Wang, C. Shi, L. Li, H. Qin, J. Hu, Sensing mechanism of SnO$_2$(110) surface to H$_2$: Density functional theory calculations, Sens. Actuators B-Chem. 220 (2015) 279–287.

[67] X. Wang, H. Qin, Y. Chen, J. Hu, Sensing Mechanism of SnO$_2$ (110) Surface to CO: density functional theory calculations, J. Phys. Chem. C 118 (2014) 28548–28561.

[68] M. Lin, B. An, N. Niimi, Y. Jikihara, T. Nakayama, T. Honma, T. Takei, T. Shishido, T. Ishida, M. Haruta, T. Murayama, Role of the acid site for selective catalytic oxidation of NH$_3$ over Au/Nb$_2$O$_5$, ACS Catalysis 9 (2019) 1753–1756.

[69] Q. Zhang, H. Wang, P. Ning, Z. Song, X. Liu, Y. Duan, In situ DRIFTS studies on CuO-Fe$_2$O$_3$ catalysts for low temperature selective catalytic oxidation of ammonia to nitrogen, Appl. Surf. Sci. 419 (2017) 733–743.

[70] H. Wang, Q. Zhang, T. Zhang, J. Wang, G. Wei, M. Liu, P. Ning, Structural tuning and NH$_3$-SCO performance optimization of CuO-Fe$_2$O$_3$ catalysts by impact of thermal treatment, Appl. Surf. Sci. 485 (2019) 81–91.

[71] H. Wang, P. Ning, Q. Zhang, X. Liu, T. Zhang, J. Fan, J. Wang, K. Long, Promotional mechanism of WO$_3$ over RuO$_2$-Fe$_2$O$_3$ catalyst for NH$_3$-SCO reaction, Appl. Catal. A: Gen. 561 (2018) 158–167.

[72] H. Wang, R. Zhang, Y. Liu, P. Li, H. Chen, F.R. Wang, W.Y. Teoh, Selective catalytic oxidation of ammonia over nano Cu/zeolites with different topologies, Environ. Sci. Nano 7 (2020) 1399–1414.

[73] G.S. Qi, R.T. Yang, R. Chang, MnO$_x$-CeO$_2$ mixed oxides prepared by co-precipitation for selective catalytic reduction of NO with NH$_3$ at low temperatures, Appl. Catal. B-Environ. 51 (2004) 93–106.